Check for updates

View Article Online
View Journal

Nanoscale

Accepted Manuscript

This article can be cited before page numbers have been issued, to do this please use: S. Madhu, S. Kokilavani, U. Sohail, M. K. Chhina and G. S. Selopal, *Nanoscale*, 2026, DOI: 10.1039/D6NR01274D.

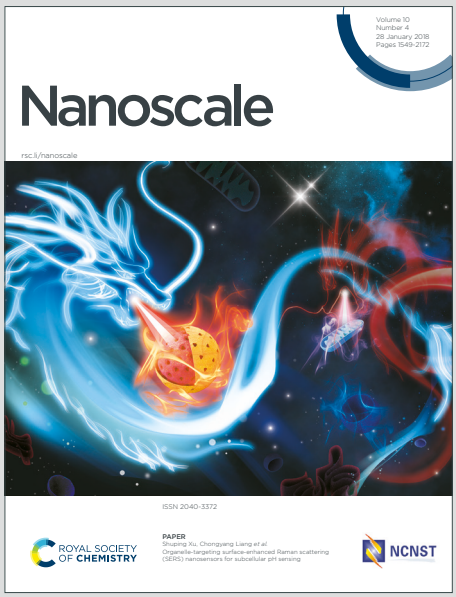

This is an Accepted Manuscript, which has been through the Royal Society of Chemistry peer review process and has been accepted for publication.

Accepted Manuscripts are published online shortly after acceptance, before technical editing, formatting and proof reading. Using this free service, authors can make their results available to the community, in citable form, before we publish the edited article. We will replace this Accepted Manuscript with the edited and formatted Advance Article as soon as it is available.

You can find more information about Accepted Manuscripts in the Information for Authors.

Please note that technical editing may introduce minor changes to the text and/or graphics, which may alter content. The journal's standard Terms & Conditions and the Ethical guidelines still apply. In no event shall the Royal Society of Chemistry be held responsible for any errors or omissions in this Accepted Manuscript or any consequences arising from the use of any information it contains.

ROYAL SOCIETY OF CHEMISTRY

rsc.li/nanoscale

View Article Online
DOI: 10.1039/D6NR01274D

Dual-Functional Heavy-Metal-free Quantum Dots/TiO_2 Hybrid System for Simultaneous Pollutant Degradation and Green Hydrogen Production

Swedha Madhu[a],Shanmugasundaram Kokilavani [a], Umair Sohail[a], Manmeet Kaur Chhina[a], Gurpreet Singh Selopal[a]*

[a] Sustainable Nanoengineering Lab, Department of Engineering, Faculty of Agriculture, Dalhousie University, Truro, B2N 5E3, NS, Canada.

Corresponding author: Gurpreet Singh Selopal, E-mail: gs.selopal@dal.ca

Open Access Article. Published on 24 June 2026. Downloaded on 6/29/2026 1:12:21 PM.
This article is licensed under a Creative Commons Attribution-NonCommercial 3.0 Unported Licence.

Abstract. Solar-driven photoelectrochemical (PEC) systems have emerged as a sustainable and cost-effective strategy for wastewater remediation and green hydrogen (H_2) production; however, integrated systems that valorize organic pollutants and generate green H_2 are underexplored. Herein, we report a heavy-metal-free Mn-doped $CuInSe_2$ (Mn:$CuInSe_2$) quantum dots (QDs) engineered mesoporous TiO_2 hybrid photoanode for simultaneous organic pollutant degradation and H_2 evolution within a single bias-assisted PEC configuration. The Mn:$CuInSe_2$ QDs absorb a broader visible light range and enhanced charge-transfer rate. The Mn:$CuInSe_2$/TiO_2 interface promotes efficient carrier separation and suppresses recombination through favorable band alignment and rapid interfacial electron injection. Under optimized conditions, the Mn:$CuInSe_2$/TiO_2 hybrid photoanode achieves 93.31% degradation of Rhodamine B (RhB) at 1.4 V vs. RHE and a photocurrent density of 2.58 mA cm^{-2} at 1 V vs. RHE, leading to a H_2 generation rate of ~48.5 µmol $h^{-1}cm^{-2}$, which is 25 times higher than bare TiO_2 device under 1 sun illumination (AM 1.5G, 100 mW/cm^2). The Mn:$CuInSe_2$/TiO_2 hybrid system exhibits excellent recyclability and stable photocurrent over 7200 s. This work establishes a robust QDs-TiO_2 hybrid design for efficient solar-driven wastewater treatment and clean H_2 production, suitable for scalable applications.

Keywords: Quantum dots; Hybrid photoanode; Photocatalysis; Carrier dynamics; Photoelectrochemical degradation; Hydrogen generation.

Nanoscale Accepted Manuscript

View Article Online
DOI: 10.1039/D6NR01274D

Open Access Article. Published on 24 June 2026. Downloaded on 6/29/2026 1:12:21 PM.
This article is licensed under a Creative Commons Attribution-NonCommercial 3.0 Unported Licence.

Nanoscale Accepted Manuscript

1. Introduction

On Earth, freshwater reserves (<1% of Earth's total water) are in a critical state of crisis due to over-abstraction faster than natural replenishment to support population growth and urbanization [1]. To meet the targets set by the United Nations (UN) Sustainable Development Goals, accelerating current efforts on access to clean water and energy requires developing scalable and efficient technologies that can simultaneously address energy scarcity and environmental pollution [2]. Numerous conventional wastewater treatments have been employed, including biological treatments (activated sludge)[3], adsorption[4], filtration, coagulation, and chemical co-precipitation [5]. However, complex operations, secondary waste/sludge generation, and incomplete mineralization limit the efficiency of these systems. In parallel, the depletion of fossil fuels and the environmental consequences of their use, such as greenhouse gas (GHG) emissions and global warming, have accelerated the transition to clean, renewable energy sources. Hydrogen (H_2) has emerged as a promising sustainable fuel owing to its high energy density and zero carbon emissions upon combustion in a fuel cell. Solar-driven photoelectrochemical (PEC) advanced oxidation of organic pollutants are efficient and sustainable approach [6, 7]. The strong oxidizing species ($^{\bullet}OH$, $^{\bullet}O_2^-$) generated from PEC systems directly mineralize the complex pollutants into CO_2, H_2O and inorganic ions. Recently, PEC systems for simultaneous H_2 production and wastewater treatment have been explored due to the high organic content (electron donors) in wastewater, and producing H_2 offsets treatment costs [8].

In a PEC system, illumination of the photoelectrode generates photoinduced charge carriers, electrons (e^-) and holes (h^+), which are efficiently separated under an applied bias. These e^- are driven toward the external circuit for H_2 evolution reaction (HER) [7]. Concurrently, the photogenerated h^+ migrate to the photoanode surface for generating highly reactive oxygen species (ROS) such as hydroxyl radicals (•OH) that facilitate the oxidation of organic pollutants

View Article Online
DOI: 10.1039/D5NR01274D

Open Access Article. Published on 24 June 2026. Downloaded on 6/29/2026 1:12:21 PM.
This article is licensed under a Creative Commons Attribution-NonCommercial 3.0 Unported Licence.

Nanoscale Accepted Manuscript

[9]. Several metal oxide semiconductors, including TiO_2, ZnO, Fe_2O_3, WO_3 have been widely employed in these PEC systems due to their chemically inert, high thermal stability, redox potential alignment, low-cost, non-toxic and abundance [10]. However, wide band gap metal oxide semiconductors have wide band gap, which limits the solar light absorption (UV region of <5% of solar spectrum) [11]. Therefore, broadening the light absorption into the visible regions is crucial for harvesting maximum photons to efficiently drive the photo-induced redox reactions. To address this, extensive research has focused on integrating wide bandgap metal oxides with photosensitizers to enable the harvesting of a broader spectrum of solar radiation and achieve improved efficiency [12, 13].

Quantum dots (QDs) have been widely used as light harvesters with metal oxides to boost light absorption. Thanks to quantum confinement effects, the size/shape/composition can be tailored to alter the band gap for broader light absorption to maximize overlap with solar spectrum [14, 15]. In addition, the high-absorption co-efficient, high photoluminescence quantum yield (PLQY), hot carrier generation[16] and multiple electron generation[17]. It's crucial to note that the high-performing QDs are toxic, namely, PbS[18], CdS [19], and CdSe [20], limiting the real-time applications. As an alternative, various heavy metal-free QDs have been developed, including AgInSe [21], InP [22], ZnSe [23], and ZnInSe [24]. The Cu-based chalcopyrite ternary colloidal QDs (I-III-VI), CuInSe [25], CuInS [26], $Cu_{2-x}Se$ QDs [27], are widely explored due to broad light window (upto NIR range), large stokeshift (difference between absorption maximum and minimum), composition-tunable band gap, and high PL lifetime. Transition metal ions such as Cu, Mn, Ag are used as dopants to introduce new optical and electronic properties. For instance, optimized Mn-dopant concentration (2% Mn^{2+}) improved PLQY (43.2%) on ZnSe/ZnS core/shell QDs[28]. Guilin et al. tuned Mn/In ratio to obtain dual emissions (intrinsic emission from host and Mn-doped emission) in Mn:InP/ZnSe QDs using a growth-doping strategy [29].

View Article Online
DOI: 10.1039/D6NR01274D

Open Access Article. Published on 24 June 2026. Downloaded on 6/29/2026 1:12:21 PM.
This article is licensed under a Creative Commons Attribution-NonCommercial 3.0 Unported Licence.

Herein, we explored the Mn-doped $CuInSe_2$ QDs (Mn:$CuInSe_2$)/TiO_2 hybrid thin-film photoanode for concurrent PEC oxidation of Rhodamine B (RhB) and H_2 generation. The synthesized nanohybrid was characterized using a range of physicochemical techniques to verify its structural, morphological, optical, and electronic properties. The engineered Mn:$CuInSe_2$/TiO_2 interface facilitates efficient charge separation, suppressing electron-hole recombination through favourable band alignment. The systematic variation of the applied voltage revealed an optimal bias condition for maximizing charge separation and minimizing recombination. Under optimized conditions (1.4 V vs. RHE), the hybrid photoanode achieves 93.31% RhB degradation in 240 min, a photocurrent density of 2.58 mA cm^{-2} at 1 V vs. RHE, and a hydrogen generation rate of ~48.5 μmol h^{-1} cm^{-2}, which is 25 times higher than bare TiO_2. In addition, the role of QD sensitization on TiO_2 was assessed by comparing photocatalytic and PEC configurations, demonstrating the critical importance of interface engineering for efficient electron-hole migration. Time-resolved PL and electrochemical impedance spectroscopy (EIS) demonstrate rapid electron transfer and low charge-transfer resistance in the QDs/TiO_2 hybrid. The mesoporous thin-film architecture offers efficient material utilization, excellent recyclability, and stable photocurrents for over 7200 s. The engineered Mn:$CuInSe_2$ QDs/TiO_2 nanohybrid system is a promising bifunctional platform for simultaneous clean-fuel generation and efficient wastewater treatment.

2. Experimental Section

2.1. Materials

Selenium powder (Se, 99.99%), indium(III) acetate ($In(OAc)_3$, 99.99%), copper(II) acetate monohydrate ($Cu(OAc)_2 \cdot H_2O$, 98%), zinc acetate ($Zn(OAc)_2$, 99.99%), manganese acetate ($Mn(OAc)_2$), 1-dodecanethiol (DDT), oleylamine (OLA, 70%), tri-octylphosphine (TOP), toluene, ethanol, and Rhodamine B (RhB), titanium tetrachloride ($TiCl_4$) were obtained from

Nanoscale Accepted Manuscript

View Article Online
DOI: 10.1039/D6NR01274D

Sigma-Aldrich Inc. and used as received without further purification. Titania paste non-rutile active opaque (18NR-AO) is purchased from GreatCell Solar Materials, Australia. Fluorine-doped tin oxide-coated glass substrates (FTO, ~13 Ω/sq) were obtained from Sigma-Aldrich Inc., USA.

2.2. Preparation of Mn:$CuInSe_2$ QDs/TiO_2 hybrid photoanode

2.2.1. Synthesis of Mn:$CuInSe_2$ QDs. The Mn:$CuInSe_2$ QDs were synthesized by a one-pot hot-injection method. Initially, the Se stock solution was prepared by sonicating 1 mol selenium powder in 1.2 mL trioctylphosphine (TOP) solution. In the typical synthesis procedure, $Cu(OAc)_2.H_2O$ (1 mM), $In(OAc)_3$ (1 mM), and $Mn(OAc)_2$ (1 mM) were added in the three-necked flask along with 5 mL dodecanethiol (DDT) and 1 mL of oleylamine (OLA). The reaction temperature was set to 100°C under stirring conditions and was degassed for 30 min to remove the volatile impurities. After 30 min, the reaction temperature was further increased to 130°C to obtain a clear and transparent, yellow-colored solution. The degassing continued for another 30 min. The reaction temperature was raised to 220°C, and the degassing was replaced by a nitrogen (N_2) supply. At 220°C, the Se precursor solution was quickly injected into the reaction solution. The reaction was allowed to continue for another 20 min to allow nucleation and QDs formation. The synthesized QDs were purified by washing with a mixture of ethanol and toluene, followed by centrifugation at 4000 rpm for 10 min. This separation process was repeated two times. Finally, the precipitate was re-dispersed in toluene for further characterization and experiments.

2.2.2. Preparation of TiO_2 photoanodes. The TiO_2 photoanodes were fabricated by doctor blade method. The FTO/glass substrates were cleaned by ultrasonication using acetone and distilled water (d. H_2O) for 20 min, respectively. A layer of commercial mixed TiO_2 paste was deposited on the cleaned FTO/glass substrates and was allowed to dry at room temperature for

Open Access Article. Published on 24 June 2026. Downloaded on 6/29/2026 1:12:21 PM.
This article is licensed under a Creative Commons Attribution-NonCommercial 3.0 Unported Licence.

Nanoscale Accepted Manuscript

View Article Online
DOI: 10.1039/D6NR01274D

10 min, and was heated at 120°C for 6 min. The same process was repeated one more time to deposit another layer of TiO_2 paste. The photoanodes were calcinated at 500°C for 30 min and were allowed to cool to room temperature. The as-fabricated TiO_2 photoanodes were dipped in 50 mM $TiCl_4$ solution and were heated at 70°C for 30 min. The $TiCl_4$-treated TiO_2 photoanodes were rinsed with d. H_2O to remove the residues. Subsequently, the photoanodes were annealed at 500°C for 30 min and were allowed to gradually cool down to room temperature.

2.2.3. QDs sensitization. The fabricated TiO2 photoanodes were sensitized with Mn:CuInSe2 QDs via electrophoretic deposition (EPD). Two TiO2 photoanodes (dimensions: 2 cm × 2 cm for hydrogen production and 3 cm × 3 cm for RhB degradation) were immersed in the QD solution and configured as the positive and negative electrodes, with an interelectrode distance of 1 cm. A 200 V voltage was applied using a Keithley 6514 electrometer for 2 h. Following deposition, the photoanodes were rinsed with toluene to remove unloaded QDs.

2.2.4. ZnS coating. After the successful deposition of QDs, two layers of ZnS were deposited as a capping/protective layer using the SILAR (Successive Ionic Layer Adsorption and Reaction) technique. The 0.1 M of $Zn(CH_3COO)_2.2H_2O$ in 20 mL methanol and 0.1 M $Na_2S.9H_2O$ in (1:1 methanol: d. H_2O) were used as the Zn^{2+} and S^{2-} precursors, respectively. The fabricated Mn:$CuInSe_2$ QDs/TiO_2/FTO/glass substrates were immersed in Zn^{2+} solution (1 min) and S^{2-} solution (1 min). The photoanodes were rinsed with the respective solvents after immersion and dried with N_2 gas. The process was performed for two times to coat 2 ZnS layers.

2.3 Characterization

The microstructures of the samples, including morphology at low magnification, high-resolution images, and the corresponding selected area electron diffraction (SAED) patterns, were examined using a JEOL 2100F TEM system operated at 200 kV. TEM samples were

Open Access Article. Published on 24 June 2026. Downloaded on 6/29/2026 1:12:21 PM.
This article is licensed under a Creative Commons Attribution-NonCommercial 3.0 Unported Licence.

Nanoscale Accepted Manuscript

View Article Online
DOI: 10.1039/D6NR01274D

prepared using a standard drop-casting method. X-ray photoelectron spectroscopy (XPS) analysis was carried out using a VG Microtech MultiLab ESCA 2000 X-ray photoelectron spectrometer with a monochromatic Al Kα radiation source (photon energy of 1486.6 eV), and the obtained data were analyzed using CasaXPS software. UV–Visible absorbance spectra were recorded using a Duetta UV–Visible spectrophotometer by Horiba. Photoluminescence (PL) and transient photoluminescence (TRPL) lifetime measurements of QDs, both in solution and deposited on ZrO_2 and TiO_2 mesoporous films, were performed using a 405 nm excitation laser in an FLS1000 photoluminescence spectrometer manufactured by Edinburgh Instruments.

2.4. Photoelectrochemical (PEC) measurements

First, the PEC oxidation of dye was evaluated using RhB as model dye pollutant. The degradation experiment was carried out in a three-electrode photoelectrochemical cell, with fabricated Mn:$CuInSe_2$ QDs/TiO_2 photoanodes as the working electrode and Pt and Ag/AgCl as the counter and reference electrodes, respectively. The initial RhB dye concentration of 5 mg/L was used as an electrolyte. The electrode was connected externally to the Gamry instrument interface 1010E electrochemical workstation. The PEC degradation was tested at different initial voltages (1.0, 1.2, 1.4, and 1.6 V). The degradation of RhB was monitored by the UV-visible spectrophotometer at an interval of 1 h, an aliquot sample was withdrawn, and the UV-visible spectra were recorded to evaluate the change in initial absorbance. The photoelectrochemical degradation efficiency was evaluated by (Equation (Eqn.) 1):

$$\%\ \text{of Degradation} = {}^{(C_0 - C_t)}\!/_{C_0} \times 100 \quad (1)$$

Where C_0 is the absorbance at time '0' and 'C_t' is the absorbance at time 't'.

To assess the ability of our fabricated photoanode for PEC H_2 evolution, we also tested it using the same three-electrode system. The surface of the fabricated photoanode was covered with

Open Access Article. Published on 24 June 2026. Downloaded on 6/29/2026 1:12:21 PM.
This article is licensed under a Creative Commons Attribution-NonCommercial 3.0 Unported Licence.

Nanoscale Accepted Manuscript

View Article Online
DOI: 10.1039/D6NR01274D

epoxy resin to leave an active surface area. The PEC device was tested under standard under 1 sun illumination (AM 1.5 G and 100 mW cm^{-2}). A Si reference cell was used to check the light intensity from the light source. The PEC performance was evaluated using RhB dye degradation and 0.25 M/0.35 M Na_2S and Na_2SO_3 as hole-scavengers. The PEC performance of the fabricated photoanode was evaluated using a Gamry 1000E electrochemical workstation.

3. Results and Discussion

The schematic diagram illustrates the procedure used to synthesize Mn:$CuInSe_2$ QDs via the one-pot hot-injection method (Figure 1a). The structural properties of fabricated QDs were characterized by Transmission Electron Microscopy (TEM) and X-ray diffraction (XRD). HR-TEM images of Mn:$CuInSe_2$ QDs show the pyramidal shape of the synthesized QDs (Figure 1b and c). The inter-planar spacing of 0.33 nm corresponds to the (112) plane of the tetragonal crystalline structure of Mn:$CuInSe_2$ QDs [30] [31]. TEM image at low magnification (scale: 100 nm) reveals a homogeneous size of the synthesized QDs (Figure S1a, SI). Additionally, high-resolution TEM (HR-TEM) was performed and is shown in Figure S1b, SI, confirming the pyramidal structure of the QDs. The SAED pattern shows concentric diffraction rings indexed to the (100) and (002) planes, indicating the polycrystalline nature of the QDs (Figure S1c, SI). EDS spectra of Mn:$CuInSe_2$ QDs are shown in Figure 1d, which confirms the presence of all elements (Mn, Cu, In and Se) present in the as-synthesized QDs. From the HR-TEM images of the QDs, the average crystalline size of QDs based on the size distribution histogram was 2.3±0.5 nm (Figure 1e). The optical properties of the fabricated QDs were investigated by UV-visible absorption, PL and TRPL analysis. The UV-visible absorbance spectra of the QDs show a broad absorption in the visible light range, and the excitonic peak of the fabricated QDs is centered at 550 nm (Figure 1f) [32]. The optical bandgap of the QDs was calculated to be 2.01 eV from their UV-visible absorption spectra using the Tauc plot (Figure S2, SI) [31].

Open Access Article. Published on 24 June 2026. Downloaded on 6/29/2026 1:12:21 PM.
This article is licensed under a Creative Commons Attribution-NonCommercial 3.0 Unported Licence.

Nanoscale Accepted Manuscript

View Article Online
DOI: 10.1039/D6NR01274D

Open Access Article. Published on 24 June 2026. Downloaded on 6/29/2026 1:12:21 PM.
This article is licensed under a Creative Commons Attribution-NonCommercial 3.0 Unported Licence.

Nanoscale Accepted Manuscript

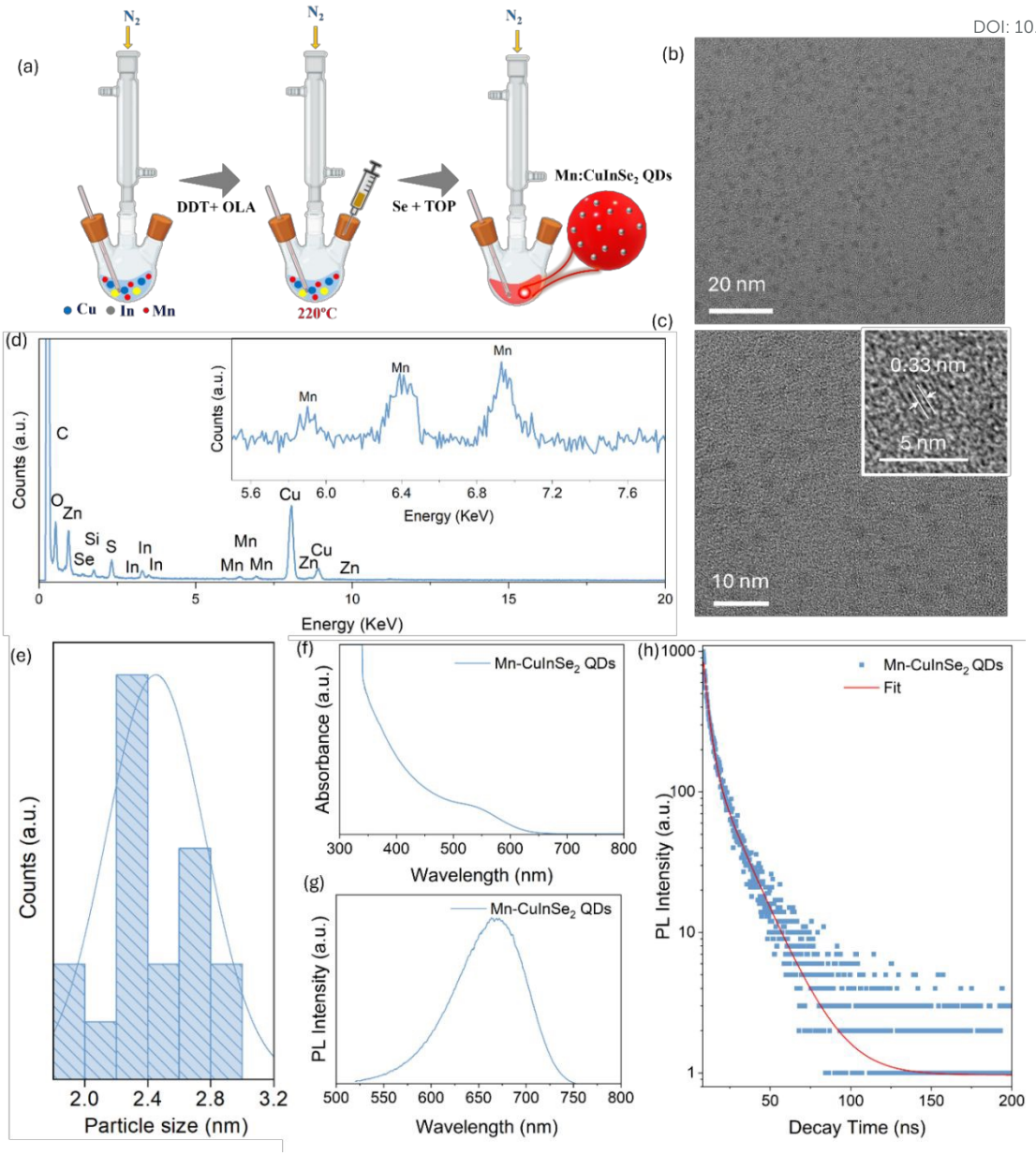

Figure 1 (a) Schematic illustration of synthesis of Mn:$CuInSe_2$ QDs, Structural analysis of Mn:$CuInSe_2$ QDs: HR-TEM image of QDs (b) at 20 nm, (c) at 10 nm, (d) elemental analysis of QDs, (e) size distribution of Mn:$CuInSe_2$ QDs with the fitting curve, (f) UV-Visible absorption spectra, (g) PL spectra, and (h) TRPL spectra QDs in toluene.

The PL spectra of Mn:$CuInSe_2$ QDs exhibit PL emission peak at 660 nm (Figure 1g). Further, to examine the charge carrier dynamics, TRPL spectroscopy was performed. Time-resolved PL decay was fitted using a tri-exponential function to obtain the average PL lifetime by the following equation (Eqn. 2),

$$\tau = \frac{a_1\tau_1^2 + a_2\tau_2^2 + a_3\tau_3^2}{a_1\tau_1 + a_2\tau_2 + a_3\tau_3} \quad (2)$$

View Article Online
DOI: 10.1039/D6NR01274D

Where 'a' is the co-efficient of the fitting and the 'τ' is the lifetime of the photogenerated charge carriers.

In general, the PL lifetime can be addressed by three main characteristics: (1) Non-radiative charge recombination, (2) Radiative process of photogenerated charge recombination, and (3) Energy transfer process [33]. The TRPL decay curve of the fabricated Mn:$CuInSe_2$ QDs, along with the fitting, were depicted. The average lifetime of the photogenerated charge carriers of the QDs was calculated to be 98.5 ns (Figure 1h).

The QDs/TiO_2 hybrid photoanode was fabricated by sensitizing Mn:$CuInSe_2$ QDs on the TiO_2 photoanodes by EPD [33] (detailed information is provided in the experimental section) (Figure 2a).

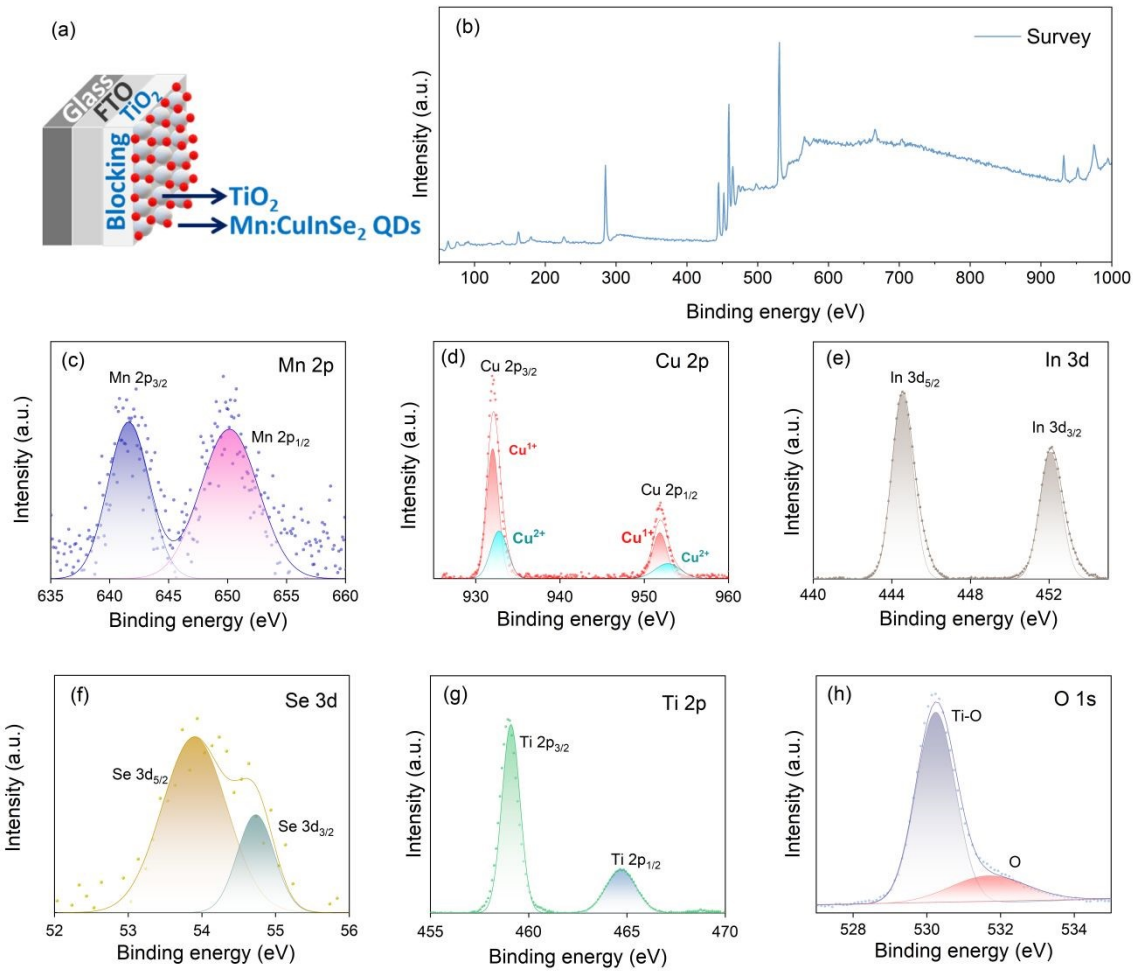

Open Access Article. Published on 24 June 2026. Downloaded on 6/29/2026 1:12:21 PM.
This article is licensed under a Creative Commons Attribution-NonCommercial 3.0 Unported Licence.

Nanoscale Accepted Manuscript

View Article Online
DOI: 10.1039/D6NR01274D

Figure 2 (a) Schematic illustration of fabricated Mn:$CuInSe_2$ QDs/TiO_2/FTO substrate, (b) XPS survey spectrum, XPS spectra of (c) Mn 2p, (d) Cu 2p, (e) In 3d, (f) Se 3d, (g) Ti 2p, and (h) O 1s of Mn:$CuInSe_2$ QDs/TiO_2.

To evaluate the chemical composition and valence oxidation states of QDs/TiO_2 hybrid, X-ray photoelectron spectroscopy (XPS) was conducted. The as-collected XPS spectra were fitted by a Gaussian distribution using Origin software. The XPS survey spectrum of the fabricated Mn:$CuInSe_2$ QDs/TiO_2 photoanodes revealed the presence of Mn, Cu, In, Se, Ti, and O elements. The XPS spectrum of Mn shows the presence of two peaks, corresponding to the Mn^{2+} oxidation state of Mn in the sample (Figure 2c) [34]. High-resolution XPS spectrum of Cu is depicted in Figure 2d. The spectrum was deconvoluted into four peaks with two main peaks corresponding to Cu $2p_{3/2}$ and Cu $2p_{1/2}$ [35, 36]. This implies that Cu in the sample is present in two valence states. The two peaks centered at 931.5 and 951.4 eV correspond to the valence state of Cu^+ state. And the other two sub peaks 932.9 and 952.8 eV correspond to the Cu^{2+} valence state. The fabricated photoanodes exhibited an increased amount of Cu^+ valence state when compared to the valence state of Cu^{2+}. This implies that the Cu present in the QDs sample is monophasic [37]. The XPS spectra of In 3d (Figure 2e) depicts the presence of four peaks, with two main peaks located at 444.6 and 452. 2 eV corresponding to the In $3d_{5/2}$ and In $3d_{3/2,}$ respectively, and two sub-peaks centered at 445.9 and 453.6 eV [38]. The sub-peaks imply that there is a slight oxidation of In in the sample, this might be due to the exposure to the ambient oxygen. The XPS spectrum of Se (Figure 2f) depicts two peaks, 53.6 and 54.5 eV, that correspond to Se $3d_{5/2}$ and Se $3d_{3/2}$, respectively [39]. These peaks represent the selenium-metal bonding in the photoanodes [40]. The Ti 2p XPS spectra clearly showed the presence of two peaks Ti $2p_{3/2}$ and Ti $2p_{1/2}$ peaks centered at 458.7 and 464.3 eV respectively, that corresponds to the valence state of +4 of Ti^{4+} in TiO_2 (Figure 2g) [41]. Additionally, no sub-peaks were observed in this spectrum, confirming that Ti is fully oxidized. The XPS spectrum of O1s reveals the presence of two peaks centered at 530.8 and 532.1 eV, corresponding to Ti-

Open Access Article. Published on 24 June 2026. Downloaded on 6/29/2026 1:12:21 PM.
This article is licensed under a Creative Commons Attribution-NonCommercial 3.0 Unported Licence.

Nanoscale Accepted Manuscript

View Article Online
DOI: 10.1039/D6NR01274D

O bond and oxygen vacancies (Figure 2h). Thus, the XPS analysis further confirms the successful loading of Mn:$CuInSe_2$ QDs decorated TiO_2 photoanodes.

The PEC performance of Mn:$CuInSe_2$ QDs/TiO_2 photoanodes for RhB degradation and H_2 evolution was evaluated by assessing the activity in separate and combined configuration. The PEC activity of the fabricated Mn:$CuInSe_2$ QDs/TiO_2 photoanodes were tested in terms of the degradation of the RhB dye at different voltage conditions. The degradation efficiency was evaluated using a UV-visible spectrophotometer. Initially, the PEC degradation efficiency of the TiO_2 photoanodes was tested under increasing voltage conditions, 1, 1.2, 1.4, and 1.6 V. The PEC degradation efficiency of the bare TiO_2 was found to increase with an increase in the voltage from 1.0 to 1.4 V but declined when the voltage was further increased to 1.6 V. The percentage of PEC degradation of RhB in the presence of TiO_2 photoanodes was found to be 27.60, 30.30, 39.61, and 35.45% with an applied potential of 1, 1.2, 1.4, and 1.6 V, respectively (Figure 3a). The corresponding C/C_0 and LnC/C_0 is depicted in Figure S3a and b, SI.

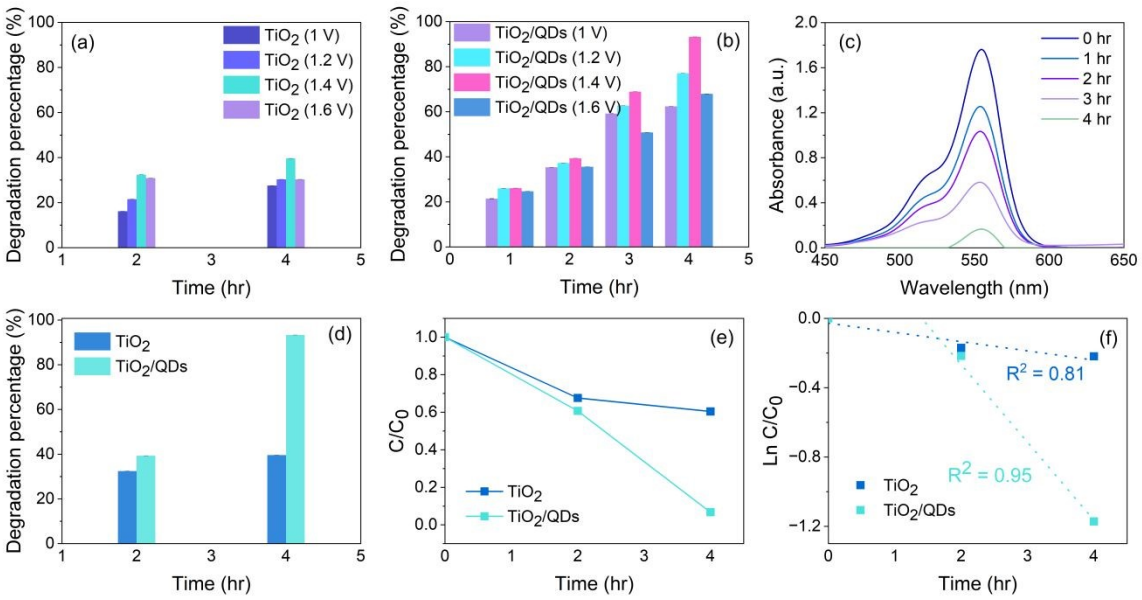

Figure 3 (a) Percentage of degradation of RhB by TiO_2 at different voltages, (b) Percentage of degradation of RhB by Mn:$CuInSe_2$ QDs/TiO_2 at increasing voltages, (c) UV-Vis-NIR spectra of degradation of RhB by Mn:$CuInSe_2$ QDs/TiO_2 at 1.4 V, (d) Comparative representation of degradation of RhB by TiO_2 and Mn:$CuInSe_2$ QDs/TiO_2: (e) C/C_0 and (f) LnC/C_0 .

Open Access Article. Published on 24 June 2026. Downloaded on 6/29/2026 1:12:21 PM.
This article is licensed under a Creative Commons Attribution-NonCommercial 3.0 Unported Licence.

Nanoscale Accepted Manuscript

View Article Online
DOI: 10.1039/D6NR01274D

Open Access Article. Published on 24 June 2026. Downloaded on 6/29/2026 1:12:21 PM.
This article is licensed under a Creative Commons Attribution-NonCommercial 3.0 Unported Licence.

Further, the Mn:$CuInSe_2$ QDs sensitized TiO_2 photoanodes were tested for the PEC degradation of RhB under the same conditions. The PEC degradation efficiency of the fabricated eco-friendly Mn:$CuInSe_2$ QDs/TiO_2 photoanodes was also tested under varying voltage conditions. The degradation of RhB was found to be increasing with the increase in voltage. The degradation efficiency of Mn:$CuInSe_2$ QDs/TiO_2 photoanodes at 1, 1.2, and 1.4 V were 65.31, 77.07, and 93.31% (Figure 3b). The PEC degradation of RhB was found to be decreasing by further increasing the voltage to 1.6 V. The corresponding C/C_0 and LnC/C_0 is depicted in Figure S3c and d, SI. The UV-vis absorption spectra for the PEC degradation of RhB by Mn:$CuInSe_2$ QDs/TiO_2 photoanodes at 1.4 V were depicted, which clearly shows that the spectra of RhB dye almost diminished after 4 h of interaction with the fabricated photoanode (Figure 3c). The degradation efficiency of Mn:$CuInSe_2$ QDs/TiO_2 compared with TiO_2 is depicted in Figure 3d. The C/C_0 and LnC/C_0 were plotted to understand the kinetics of the reaction (Figure 3e and f).

The degradation of RhB in the presence of TiO_2 photoanodes was also tested in the presence of light without any external potential supply (photocatalysis). After 4h of light irradiation, the fabricated TiO_2 photoanodes attained a degradation efficiency of 9.22%, while in the presence of an external potential bias, the PEC degradation efficiency was 27.60% (Figure 4a), and the corresponding C/C_0 and LnC/C_0 plots are depicted in Figure 4b and c. The significant increase in the degradation of RhB in the presence of external voltage indicates that the applied potential significantly enhances the degradation of RhB molecules. The degradation efficiency of Mn:$CuInSe_2$ QDs/TiO_2 photoanodes was also tested in the absence of external potential (photocatalysis condition); the degradation efficiency was nearly halved compared to the PEC condition (Figure 4d). The kinetics were studied by C/C_0 and LnC/C_0, depicted in Figure 4e and f. The degradation reaction in both PEC and PC systems follows pseudo-first-order kinetics, as confirmed by the high R^2 values (0.883–0.975), indicating good linear relationship

Nanoscale Accepted Manuscript

View Article Online
DOI: 10.1039/D6NR01274D

between ln(C/C_0) and reaction time and validates the kinetic model. The TiO_2/QDs composite shows a rate constant approximately 8 times higher than pristine TiO_2. The degradation rate enhancement demonstrates that incorporating QDs significantly improves reaction kinetics under applied bias. The TiO_2/QDs composite exhibits a rate constant 5 times higher than pure TiO_2 wherein QDs incorporation enhances photocatalytic activity even without applied potential (Table S1, SI).

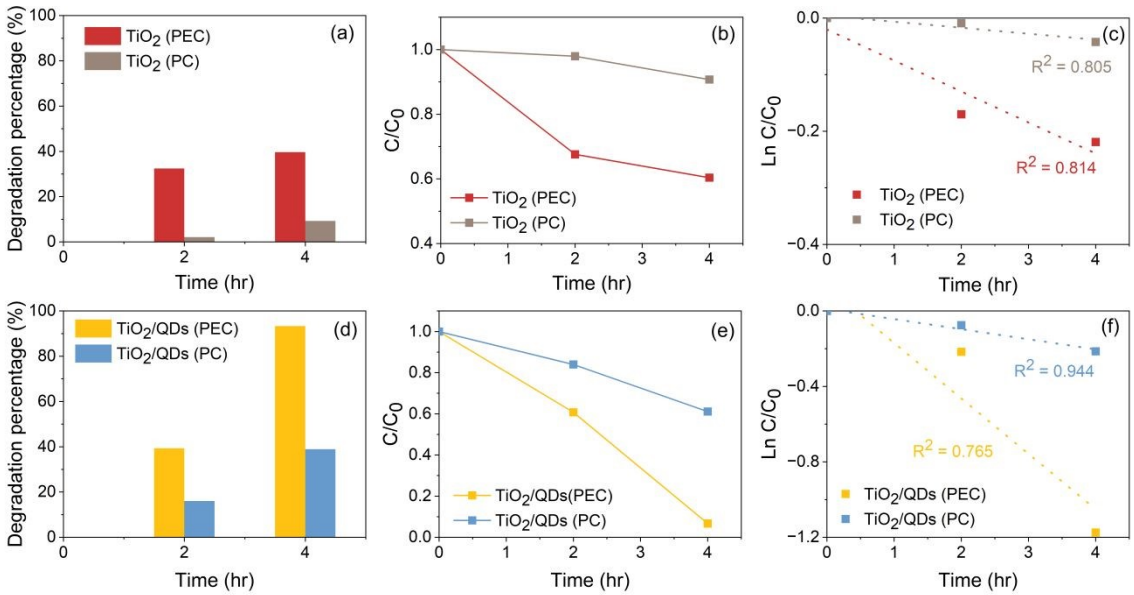

Figure 4 Comparison of degradation of RhB by TiO_2 and Mn:$CuInSe_2$ QDs/TiO_2 under PEC and PC conditions (PEC-Photoelectrochemical degradation and PC-Photocatalysis) (a) Percentage of degradation of RhB by TiO_2 under PEC and PC conditions, corresponding (b) C/C_0, (c) Ln C/C_0, (d) Percentage of degradation of RhB by Mn:$CuInSe_2$ QDs/TiO_2 under PEC and PC conditions, corresponding (e) C/C_0 and (f) Ln C/C_0.

The experiment was also repeated to ensure repeatability. The UV-vis spectra of the triplicates are depicted in Figure S4, SI, and the corresponding percentage of degradation, C/C_0 and Ln C/C_0 are represented in Figure S5, SI. To evaluate the stability of the fabricated QDs-TiO_2 photoanode, the degradation experiment was repeated for three consecutive cycles using the same QDs-TiO_2 photoanode. After each cycle, the QDs-TiO_2 photoanode was removed, washed and reused in the reaction solution for the subsequent degradation reaction test. The photoanode retained a high degradation efficiency of 91.83% after three cycles, showing only minimal performance loss compared to the initial cycle. These results confirm the good

Open Access Article. Published on 24 June 2026. Downloaded on 6/29/2026 1:12:21 PM.
This article is licensed under a Creative Commons Attribution-NonCommercial 3.0 Unported Licence.

Nanoscale Accepted Manuscript

View Article Online
DOI: 10.1039/D6NR01274D

stability, durability, and reusability of the QDs-TiO_2 photoanode for photoelectrochemical degradation of pollutants. The corresponding C/C_0 vs time for all cycles is shown in Figure S6, SI.

The fabricated Mn:$CuInSe_2$ QDs/TiO_2 photoanodes were also tested for the PEC H_2 evolution activity. Before the PEC H_2 evolution test, the fabricated Mn:$CuInSe_2$ QDs/TiO_2 photoanodes were coated with a ZnS shell via the SILAR approach. The PEC H_2 evolution was tested at dark, light, and chopped conditions using a three-electrode system. The current density was obtained with the applied potential. From the Figure, it can be seen that in the dark, there was no current observed. PEC device with TiO_2 photoanodes produced a photocurrent density of 0.10 mA cm^{-2}, with an applied potential of 1.0 V vs RHE (Figure 5a). The sensitization of TiO_2 with Mn:$CuInSe_2$ QDs has significantly improved the photocurrent density to 2.58 mA cm^{-2} at a potential of 1.0 V vs RHE (Figure 5b). The photocurrent density of the PEC device with Mn:$CuInSe_2$ QDs/TiO_2 is approximately 25 times higher than that of the PEC device with TiO_2 and is depicted in Figure 5c. Using the photocurrent density of the PEC device and Faraday's law of electrolysis, the theoretical H_2 generation rate was estimated using an active photoanode area of 1 cm^2 according to the relation:

$$\eta_{H_2} = \frac{J \times A \times t}{2F}$$

where J is the photocurrent density, A is the active electrode area, t is the reaction time, and F is the Faraday constant [42]. Based on the significantly enhanced photocurrent density of the Mn:$CuInSe_2$ QDs/TiO_2 PEC device, which was approximately 25 times higher than that of pristine TiO_2, the theoretical H_2 evolution rate was calculated to be ~48.5 μmol h^{-1} cm^{-2} under the assumption of 100% Faradaic efficiency (FE). This assumption implies that all photogenerated electrons are fully utilized for proton reduction to produce H_2 with no losses due to charge recombination, parasitic reactions, or competing side reactions. Therefore, the

Open Access Article. Published on 24 June 2026. Downloaded on 6/29/2026 1:12:21 PM.
This article is licensed under a Creative Commons Attribution-NonCommercial 3.0 Unported Licence.

Nanoscale Accepted Manuscript

View Article Online
DOI: 10.1039/D6NR01274D

Open Access Article. Published on 24 June 2026. Downloaded on 6/29/2026 1:12:21 PM.
This article is licensed under a Creative Commons Attribution-NonCommercial 3.0 Unported Licence.

reported H_2 generation value represents the maximum theoretical H_2 production rate (upper-limit estimate) rather than the experimentally measured Faradaic efficiency under practical operating conditions. Additionally, the PEC H_2 evolution with TiO_2 and Mn:$CuInSe_2$ QDs/TiO_2 photoanodes was also tested in the presence of an electrolyte containing 0.25 M Na_2S and 0.35 M Na_2SO_3 (pH=12.5) as an electrolyte and is depicted in Figure S7a and b, SI, respectively. A PEC device with Mn:$CuInSe_2$ QDs/TiO_2 photoanodes yields a photocurrent density of 3.90 mA.cm^{-2} at a potential of 1V vs RHE, which is 6.6 times higher than the PEC device with TiO_2 (0.59 mA cm^{-2} at a potential of 1V vs RHE) under one sun illumination (1.5 G and 100 mW cm^{-2}). The enhanced PEC hydrogen production performance of the Mn:$CuInSe_2$ QDs/TiO_2-based device in the presence of Na_2S/Na_2SO_3 electrolyte can be attributed to the role of sulphide/sulphite species as highly efficient sacrificial hole scavengers [43]. The Na_2S/Na_2SO_3 system facilitates rapid charge separation by effectively consuming photogenerated holes at the photoanode/electrolyte interface, thereby suppressing electron-hole recombination. In addition, the alkaline sulphide/sulphite electrolyte improves interfacial charge-transfer kinetics and promotes electron accumulation, enhancing electron availability for hydrogen evolution at the counter electrode.

The long-term stability was also evaluated by conducting chronoamperometry, where the photoanode was continuously illuminated by the light source, and the current density was continuously monitored. It can be seen that the photocurrent density was unaltered even after 7200s, indicating the excellent stability of the catalyst (Figure S8, SI). The camera picture of the PEC experimental setup and the PEC cell are depicted in Figure S9a and b, SI, respectively. The camera images of the prepared photoanode are shown in Figures S9c and d, SI.

Nanoscale Accepted Manuscript

View Article Online
DOI: 10.1039/D6NR01274D

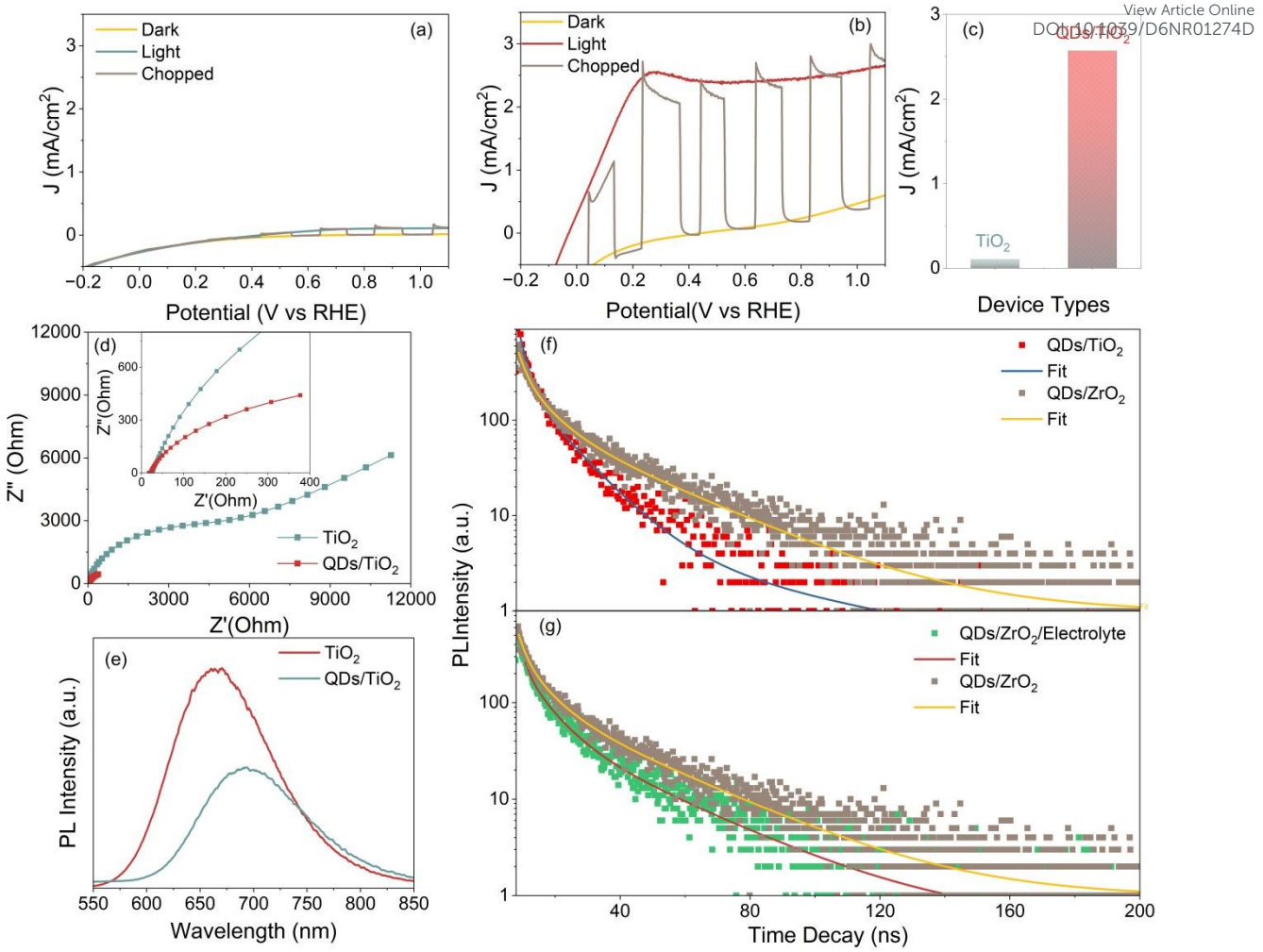

Figure 5 Photocurrent density vs potential (V vs RHE) of PEC device with: (a) TiO_2, (b) Mn:$CuInSe_2$ QDs/TiO_2. (c) Comparison of the photocurrent density of corresponding PEC devices under one sun illumination (1.5 G and 100 mW cm^{-2}). (d) EIS spectra of PEC devices based on TiO_2 and Mn:$CuInSe_2$ QDs/TiO_2. (e) PL spectra of Mn:$CuInSe_2$ QDs and Mn:$CuInSe_2$ QDs/TiO_2. Comparison of TRPL spectra of: (f) Mn:$CuInSe_2$ QDs/TiO_2 and Mn:$CuInSe_2$ QDs/ZrO_2, and (g) Mn:$CuInSe_2$ QDs/ZrO_2 with and without electrolyte condition.

The charge separation and migration dynamics of the photogenerated carriers were examined using PL spectroscopy and electrochemical impedance spectroscopy (EIS). EIS spectroscopy was employed to assess charge carrier migration efficiency. Typically, the arc radius of the semicircle in an EIS spectrum corresponds to the charge transfer resistance (R_{ct}) of the material, where a smaller arc radius indicates lower charge transfer resistance and more efficient charge migration [44]. As shown in the EIS spectra of the fabricated nanomaterial, the Mn:$CuInSe_2$ QDs/TiO_2 heterostructure exhibited a smaller semicircle radius compared to TiO_2, confirming its lower charge transfer resistance (Figure 5d). Since a larger arc radius signifies higher charge

Open Access Article. Published on 24 June 2026. Downloaded on 6/29/2026 1:12:21 PM.
This article is licensed under a Creative Commons Attribution-NonCommercial 3.0 Unported Licence.

Nanoscale Accepted Manuscript

View Article Online
DOI: 10.1039/D6NR01274D

Open Access Article. Published on 24 June 2026. Downloaded on 6/29/2026 1:12:21 PM.
This article is licensed under a Creative Commons Attribution-NonCommercial 3.0 Unported Licence.

transfer resistance and slower interfacial charge movement, these findings validate that the nanohybrid facilitates faster charge transfer, thereby enhancing the photocatalytic degradation of pollutant molecules and H_2 production. The PL emission spectra of the Mn:$CuInSe_2$ QDs and the Mn:$CuInSe_2$ QDs/TiO_2 were depicted, revealing that the PL intensity of the heterostructure was significantly reduced compared to pristine QDs (Figure 5e). This reduction indicates lower charge recombination in the nanohybrid, suggesting that the formation of the Mn:$CuInSe_2$ QDs/TiO_2 heterostructure enhances electron-hole separation and migration [45]. Consequently, the incorporation of QDs improves interactions with ambient molecules, leading to enhanced photocatalytic degradation efficiency.

The TRPL decay spectra was utilized to further investigate the formation and migration dynamics of photogenerated charge carriers (Figure 5f-g). To understand carrier recombination dynamics, the QDs were sensitized on TiO_2 and ZrO_2 films, and TRPL spectra were measured both with and without an electrolyte. The carrier dynamics of photogenerated e^- and h^+ pairs in QDs are governed by the optimized band alignment between the CB of the TiO_2 mesoporous film and that of the QDs, as well as the alignment between the redox potential of the polysulfide electrolyte and the VB edge of the QDs. In contrast, the CB of wide band gap ZrO_2 (Eg = 5 eV) is more negative than the CB of the QDs [46], the chances of e^- transfer rate from photoexcited QDs to ZrO_2 in QDs/ZrO_2 are lower than that in QDs/TiO_2 nanohybrid and therefore serve as a benchmark for comparison [47]. The average PL lifetime of photogenerated charges decreases from 98.5 ns for Mn:$CuInSe_2$ QDs to 11.1 ns for Mn:$CuInSe_2$ QDs/TiO_2, indicating the rapid electron transfer at the interface of Mn:$CuInSe_2$ QDs/TiO_2 nanohybrid. The average lifetime of QDs/TiO_2 is shorter than that of QDs/ZrO_2, indicating that the charge transfer from QDs to TiO_2 is efficient due to the suitable band alignment (Figure 5f). The QDs/ZrO_2 had a shorter lifetime in the presence of electrolyte, indicating the faster hole transfer to the electrolyte (Figure 5g). The shorter decay lifetime signifies a faster interfacial charge

Nanoscale Accepted Manuscript

View Article Online
DOI: 10.1039/D6NR01274D

transfer through non-radiative quenching pathways [48]. The TRPL decay spectra further confirms that QDs enhance electron transfer by facilitating rapid electron consumption. In addition, the K_{et} and K_{ht} are calculated from the difference in the carrier lifetime values with ZrO_2 and TiO_2 by using the following equation (Eqn. 3)

$$K_{et/ht} = \frac{1}{<\tau>QDs/TiO_2\ /solvent} - \frac{1}{<\tau>QDs/ZrO_2} \quad (3)$$

Where τ QDs/TiO_2 and τ QDs/ZrO_2 represent the average lifetime of QDs in the presence of TiO_2 and solvent, and on a ZrO_2 mesoporous film, respectively. The K_{et} from the CB of Mn:$CuInSe_2$ QDs to the CB of mesoporous TiO_2 was calculated to be 3.86×10^7 s^{-1}, while the K_{ht} from the solvent to the VB of Mn:$CuInSe_2$ QDs was 2.63×10^7 s^{-1}. These values confirm the highly efficient charge carrier dynamics of the hybrid photocatalyst system.

The recent progress in PEC systems developed for simultaneous wastewater treatment and hydrogen production is summarized in Table S2. For instance, Allan et al. [49] demonstrated a $WO_3/BiVO_4$ system for municipal sewage wastewater treatment, achieving complete degradation of surfactants within 100 min along with a relatively high H_2 evolution rate of 82.51 μmol h^{-1} cm^{-2} at 1.75 V. Yu et al. [50] employed Ce-MOFs/Black-TNTs photoanode and CCM/Black-TNTs photocathode systems for degradation of 2,4-dichlorophenoxyacetic acid in industrial wastewater, achieving 98% degradation in 180 min with an H_2 evolution rate of 40 μmol h^{-1} cm^{-2} at 2.4 V vs RHE. Additionally, similar works were reported [51-54] in Table S2. Although some reported heterostructures exhibited higher hydrogen evolution rates, they generally required higher external bias potentials (≥1.75 V vs RHE), indicating increased energy consumption. Compared with these previously reported systems, the fabricated Mn:$CuInSe_2/TiO_2$ photoanode demonstrated balanced PEC performance, achieving 93.31% Rhodamine B degradation within 240 min along with an H_2 evolution rate of 48.5 μmol h^{-1} cm^{-2} at a comparatively low applied bias of 1.4 V vs RHE.

Open Access Article. Published on 24 June 2026. Downloaded on 6/29/2026 1:12:21 PM.
This article is licensed under a Creative Commons Attribution-NonCommercial 3.0 Unported Licence.

Nanoscale Accepted Manuscript

View Article Online
DOI: 10.1039/D6NR01274D

Open Access Article. Published on 24 June 2026. Downloaded on 6/29/2026 1:12:21 PM.
This article is licensed under a Creative Commons Attribution-NonCommercial 3.0 Unported Licence.

4. Photoelectrochemical degradation and H_2 production mechanism

A possible mechanism was illustrated based on the band gap, valence band (VB), and conduction band (CB) of TiO_2 and Mn:$CuInSe_2$ QDs (Figure 6). The band gap of the fabricated TiO_2 and Mn:$CuInSe_2$ QDs was calculated to be 3.05 [55] and 2.01 eV [31], respectively. The band gap of Mn:$CuInSe_2$ QDs was calculated based on the obtained UV-Visible absorbance spectra of the QDs. The VB and CB potential of the fabricated QDs was calculated using the equation given below [56] (Eqn. 4 and 5),

$$E_{CB} = X - E^c - 0.5E_g \quad (4)$$

$$E_{CB} = E_{VB} - E_g \quad (5)$$

Where E_{CB} and E_{VB} are the potential of CB and VB, X is the electronegative potential, E^c is the energy of free electrons, and E_g is the band gap of the materials. The calculated VB and CB of TiO_2 and Mn:$CuInSe_2$ QDs were calculated to be 2.6 and -0.45 eV, 0.59 and -1.31 eV, respectively. When these semiconductors are excited with photons, e^- from the VB leave and reach the CB, leaving h^+ behind in the VB. These e^- and h^+ react with the oxygen and water molecules, forming $\cdot O_2^-$ radicals and $\cdot$OH radicals.

Typically, when these Mn:$CuInSe_2$ QDs are decorated over TiO_2, there is an interfacial charge barrier between the counter semiconductors, and the band aligns till these semiconductors reach an equilibrium, forming a heterostructure. The incident photons help in exciting the e^-, forming e^-/h^+ pairs. The e^- from the QDs moves to the CB of the TiO_2 layer to nullify the Fermi level difference. There are high chances of these charge carriers recombining and reducing the photocatalytic activity. Thus, in the presence of an external electrical field from the applied bias pulls the e^- towards the FTO and further to the external circuit and reach the counter electrode, forming H_2 molecules by reducing the water molecules. On the other hand, the holes

Nanoscale Accepted Manuscript

View Article Online
DOI: 10.1039/D6NR01274D

of QDs react with the surrounding water molecules forming ·OH radicals. These ·OH radicals are highly active and react with the organic pollutant RhB molecules, forming non-toxic and smaller compounds (Figure 6). Thus, the decorated Mn:$CuInSe_2$ QDs onto the TiO_2 photoanode not only improved the visible light absorption of the heterostructure but also had a suitable band structure alignment for the charge carrier transfer and improved performance in terms of both degradation of organic pollutant RhB and H_2 generation by water splitting. Compared to previously reported systems, this Mn:$CuInSe_2$/TiO_2 QDs based photoanode operates at a moderate applied bias (1.4 V) and maintaining competitive degradation efficiency (93.31% at 240 min) and hydrogen production (48.5 μmol h^{-1} cm^{-2}). In addition, the reported systems rely on complex multi-layer oxide or MOF structures. This QDs-engineered photoanode demonstrates that semiconductor QDs can effectively enhance solar-driven pollutant degradation with hydrogen production.

Open Access Article. Published on 24 June 2026. Downloaded on 6/29/2026 1:12:21 PM.
This article is licensed under a Creative Commons Attribution-NonCommercial 3.0 Unported Licence.

Nanoscale Accepted Manuscript

View Article Online
DOI: 10.1039/D6NR01274D

Open Access Article. Published on 24 June 2026. Downloaded on 6/29/2026 1:12:21 PM.
This article is licensed under a Creative Commons Attribution-NonCommercial 3.0 Unported Licence.

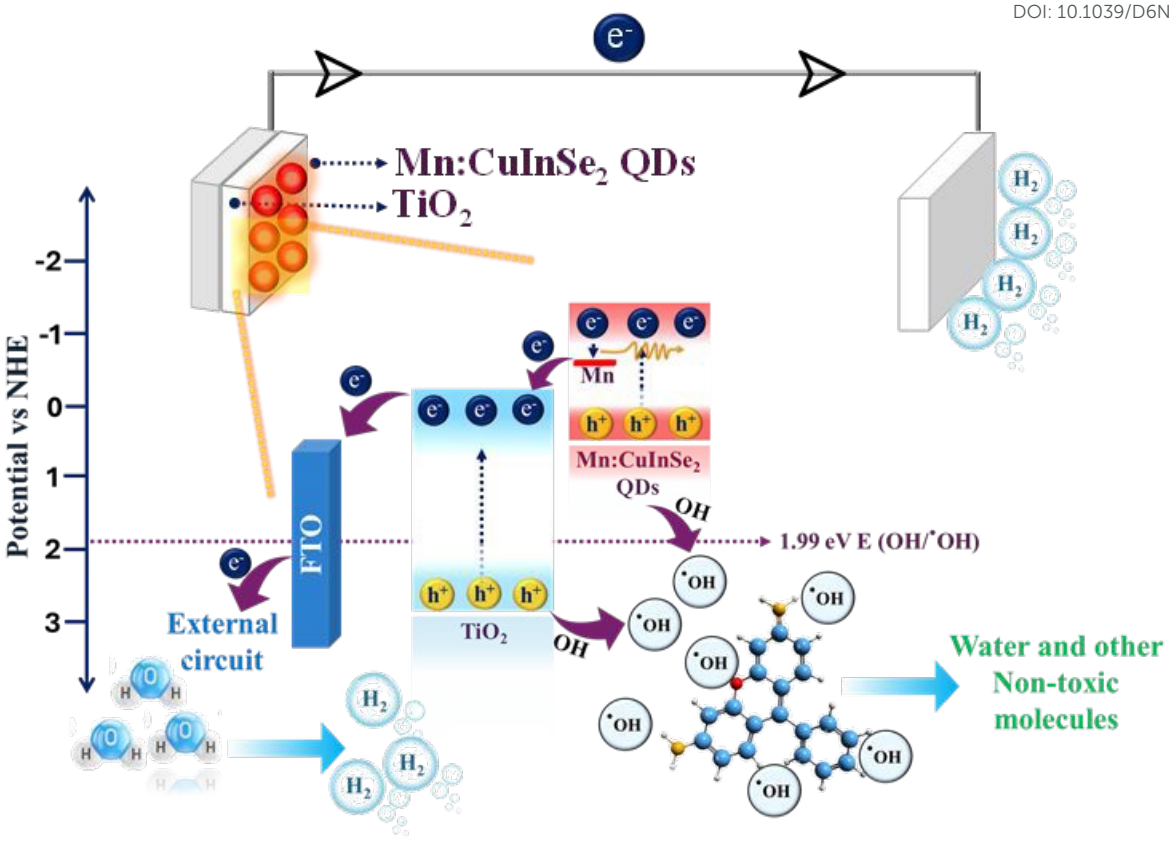

Figure 6 Schematic representation of the carrier dynamics mechanism of Mn:$CuInSe_2$ QDs/TiO_2 hybrid system for simultaneous PEC degradation of RhB and green H_2 production.

5. Conclusions

To summarize, we reported the fabrication of a novel and eco-friendly Mn:$CuInSe_2$ QDs/TiO_2 photoanodes, explored the PEC degradation of RhB, and simultaneously green H_2 production. Firstly, the photoanodes were characterized with various structural and optical characterization techniques. The fabricated Mn:$CuInSe_2$ QDs/TiO_2 photoanodes had achieved an excellent RhB degradation with a degradation efficiency of 93.31 %, compared with the bare TiO_2 photoanodes, which achieved a very low degradation efficiency of 27.6 %, indicating the improved light absorption of the QDs and a feasible charge separation and transfer between the QDs and TiO_2, which in turn improved the PEC degradation of RhB. Similarly, the PEC H_2 evolution was tested and compared between Mn:$CuInSe_2$ QDs/TiO_2 photoanodes and pristine TiO_2. The Mn:$CuInSe_2$ QDs/TiO_2 photoanodes attained a photocurrent density of ~2.60 mA

Nanoscale Accepted Manuscript

View Article Online
DOI: 10.1039/D6NR01274D

cm^{-2} at 1 V vs. RHE, approximately 25 times higher than that of the control device. The fabricated Mn:$CuInSe_2$ QDs/TiO_2 photoanode also has excellent stability, maintaining a constant current density of about 7200 s. Overall, the fabricated Mn:$CuInSe_2$ QDs/TiO_2 photoanode are an environmentally friendly, cost-effective, and highly efficient water treatment and simultaneous solar-driven H_2 production system, offering broader and more in-depth exploration of QDs in high-performance PEC applications.

Open Access Article. Published on 24 June 2026. Downloaded on 6/29/2026 1:12:21 PM.
This article is licensed under a Creative Commons Attribution-NonCommercial 3.0 Unported Licence.

Nanoscale Accepted Manuscript

Acknowledgements

G.S.S. acknowledges funding from the Natural Science and Engineering Research Council of Canada (NSERC) and the Canada Foundation for Innovation-John R. Evans Leaders Fund (CFI-JELF) for infrastructure support and its operating funds. G.S.S. acknowledges funding support from Dalhousie University. U.S. acknowledges the Killam Pre-doctoral Fellowship. K.S. acknowledges funding support from the Dalhousie Research Excellence Award and the Nova Scotia Graduate Scholarship. All authors acknowledge funding from the NSERC-SSHRC Alliance.

Conflicts of Interest

The authors declare no conflicts of interest.

References

[1] R. Kumar and S. Mathur, "Natural reserves of water on earth," in *Handbook of Research on Water Sciences and Society*: IGI Global Scientific Publishing, 2022, pp. 699-721.

[2] M. E. Demir, G. Chehade, I. Dincer, B. Yuzer, and H. Selcuk, "Synergistic effects of advanced oxidization reactions in a combination of TiO2 photocatalysis for hydrogen production and wastewater treatment applications," *International Journal of Hydrogen Energy,* vol. 44, no. 43, pp. 23856-23867, 2019.

View Article Online
DOI: 10.1039/D6NR01274D

[3] M. Henze, M. C. van Loosdrecht, G. A. Ekama, and D. Brdjanovic, *Biological wastewater treatment*. IWA publishing, 2008.

[4] S. De Gisi, G. Lofrano, M. Grassi, and M. Notarnicola, "Characteristics and adsorption capacities of low-cost sorbents for wastewater treatment: A review," *Sustainable Materials and Technologies,* vol. 9, pp. 10-40, 2016.

[5] C. Wang, K. Rong, Y. Liu, F. Yang, and S. Li, "Carbon quantum dots-modified tetra (4-carboxyphenyl) porphyrin/BiOBr S-scheme heterojunction for efficient photocatalytic antibiotic degradation," *Science China Materials,* vol. 67, no. 2, pp. 562-572, 2024.

[6] R. Kaushik, S. Gandhi, and A. Halder, "Photoelectrochemical degradation of organic pollutants coupled with molecular hydrogen generation using Bi2O3/TiO2 nanoparticle arrays," *ACS Applied Nano Materials,* vol. 6, no. 6, pp. 4297-4308, 2023.

[7] E. Mousset *et al.*, "A new 3D-printed photoelectrocatalytic reactor combining the benefits of a transparent electrode and the Fenton reaction for advanced wastewater treatment," *Journal of Materials Chemistry A,* vol. 5, no. 47, pp. 24951-24964, 2017.

[8] Z. Zheng, J. He, J. H. K. Man, T. Dong, and I. M. C. Lo, "Hydrogen production from photoelectrochemical wastewater treatment: advancing toward sustainability," *Current Opinion in Chemical Engineering,* vol. 47, p. 101096, 2025/03/01/ 2025.

[9] B. Deng, S. Fu, Y. Zhang, Y. Wang, D. Ma, and S. Dong, "Simultaneous pollutant degradation and power generation in visible-light responsive photocatalytic fuel cell with an Ag-TiO2 loaded photoanode," *Nano-Structures & Nano-Objects,* vol. 15, pp. 167-172, 2018.

[10] Y. Yang, S. Niu, D. Han, T. Liu, G. Wang, and Y. Li, "Progress in developing metal oxide nanomaterials for photoelectrochemical water splitting," *Advanced Energy Materials,* vol. 7, no. 19, p. 1700555, 2017.

Open Access Article. Published on 24 June 2026. Downloaded on 6/29/2026 1:12:21 PM.
This article is licensed under a Creative Commons Attribution-NonCommercial 3.0 Unported Licence.

Nanoscale Accepted Manuscript

View Article Online
DOI: 10.1039/D6NR01274D

[11] X. Chen, S. Shen, L. Guo, and S. S. Mao, "Semiconductor-based photocatalytic hydrogen generation," *Chemical reviews,* vol. 110, no. 11, pp. 6503-6570, 2010.

[12] S. Linic, P. Christopher, and D. B. Ingram, "Plasmonic-metal nanostructures for efficient conversion of solar to chemical energy," *Nature materials,* vol. 10, no. 12, pp. 911-921, 2011.

[13] U. Aslam, V. G. Rao, S. Chavez, and S. Linic, "Catalytic conversion of solar to chemical energy on plasmonic metal nanostructures," *Nature Catalysis,* vol. 1, no. 9, pp. 656-665, 2018.

[14] X.-B. Li, C.-H. Tung, and L.-Z. Wu, "Semiconducting quantum dots for artificial photosynthesis," *Nature Reviews Chemistry,* vol. 2, no. 8, pp. 160-173, 2018.

[15] G. S. Selopal, H. Zhao, Z. M. Wang, and F. Rosei, "Core/shell quantum dots solar cells," *Advanced Functional Materials,* vol. 30, no. 13, p. 1908762, 2020.

[16] P. Singhal and H. N. Ghosh, "Hot charge carriers in quantum dots: generation, relaxation, extraction, and applications," *ChemNanoMat,* vol. 5, no. 8, pp. 985-999, 2019.

[17] A. J. Nozik, "Multiple exciton generation in semiconductor quantum dots," *Chemical Physics Letters,* vol. 457, no. 1-3, pp. 3-11, 2008.

[18] P. Pathak, M. Podzorski, D. Bahnemann, and V. R. Subramanian, "One-pot fabrication of high coverage PbS quantum dot nanocrystal-sensitized titania nanotubes for photoelectrochemical processes," *The Journal of Physical Chemistry C,* vol. 122, no. 25, pp. 13659-13668, 2018.

[19] Z. Bai, X. Yan, Y. Li, Z. Kang, S. Cao, and Y. Zhang, "3D-branched ZnO/CdS nanowire arrays for solar water splitting and the service safety research," *Advanced Energy Materials,* vol. 6, no. 3, p. 1501459, 2016.

Open Access Article. Published on 24 June 2026. Downloaded on 6/29/2026 1:12:21 PM.
This article is licensed under a Creative Commons Attribution-NonCommercial 3.0 Unported Licence.

Nanoscale Accepted Manuscript

View Article Online
DOI: 10.1039/D6NR01274D

[20] J. Hensel, G. Wang, Y. Li, and J. Z. Zhang, "Synergistic effect of CdSe quantum dot sensitization and nitrogen doping of TiO2 nanostructures for photoelectrochemical solar hydrogen generation," *Nano letters,* vol. 10, no. 2, pp. 478-483, 2010.

[21] J. Nong *et al.*, "Eco-friendly and high-performance photoelectrochemical anode based on AgInS 2 quantum dots embedded in 3D graphene nanowalls," *Journal of Materials Chemistry C,* vol. 7, no. 32, pp. 9830-9839, 2019.

[22] S. Chandrasekaran, T. J. Macdonald, Y. J. Mange, N. H. Voelcker, and T. Nann, "A quantum dot sensitized catalytic porous silicon photocathode," *Journal of Materials Chemistry A,* vol. 2, no. 25, pp. 9478-9481, 2014.

[23] X. Tong *et al.*, "Proteomic identification of marker proteins and its application to authenticate Ophiocordyceps sinensis," *3 Biotech,* vol. 8, pp. 1-8, 2018.

[24] B. Luo *et al.*, "High efficiency photoelectrochemical hydrogen generation using eco-friendly Cu doped Zn-In-Se colloidal quantum dots," *Nano Energy,* vol. 88, p. 106220, 2021.

[25] Z. Tan *et al.*, "Near-band-edge electroluminescence from heavy-metal-free colloidal quantum dots," *Advanced materials,* vol. 23, no. 31, pp. 3553-3558, 2011.

[26] S.-H. Chen *et al.*, "Photosensitizer–conjugated Cu-In-S heterostructured nanorods for cancer targeted photothermal/photodynamic synergistic therapy," *Materials Science and Engineering: C,* vol. 97, pp. 793-802, 2019.

[27] J. S. Tsai, K. Dehvari, W. C. Ho, K. Waki, and J. Y. Chang, "In situ microwave-assisted fabrication of hierarchically arranged metal sulfide counter electrodes to boost stability and efficiency of quantum dot-sensitized solar cells," *Advanced Materials Interfaces,* vol. 6, no. 5, p. 1801745, 2019.

Open Access Article. Published on 24 June 2026. Downloaded on 6/29/2026 1:12:21 PM.
This article is licensed under a Creative Commons Attribution-NonCommercial 3.0 Unported Licence.

Nanoscale Accepted Manuscript

View Article Online
DOI: 10.1039/D0NR01274D

[28] H. Wang *et al.*, "ZnSe/ZnS Core–Shell Quantum Dots Doped with Mn2+ Ions for Magnetic State-Manipulated Light Sources," *ACS Applied Nano Materials,* vol. 5, no. 6, pp. 8448-8456, 2022/06/24 2022.

[29] G. Zhang *et al.*, "Dual-Emissive and Color-Tunable Mn-Doped InP/ZnS Quantum Dots via a Growth-Doping Method," *Nanoscale Research Letters,* vol. 13, no. 1, p. 170, 2018/06/07 2018.

[30] N. Irmania, K. Dehvari, and J.-Y. Chang, "Multifunctional MnCuInSe/ZnS quantum dots for bioimaging and photodynamic therapy," *Journal of Biomaterials Applications,* vol. 36, no. 9, pp. 1617-1628, 2022.

[31] M. A. Abate, K. Dehvari, J.-Y. Chang, and K. Waki, "Aqueous synthesis of Mn-doped CuInSe 2 quantum dots to enhance the performance of quantum dot sensitized solar cells," *Dalton Transactions,* vol. 48, no. 42, pp. 16115-16122, 2019.

[32] N. S. Karan, D. D. Sarma, R. M. Kadam, and N. Pradhan, "Doping transition metal (Mn or Cu) ions in semiconductor nanocrystals," *The Journal of Physical Chemistry Letters,* vol. 1, no. 19, pp. 2863-2866, 2010.

[33] P. Li and T. He, "Common-cation based Z-scheme ZnS@ ZnO core-shell nanostructure for efficient solar-fuel production," *Applied Catalysis B: Environmental,* vol. 238, pp. 518-524, 2018.

[34] S. Cao, C. Dai, J. Zhao, and B. Zou, "Synthesis of dual-emission Ag-and Mn-codoped Zn-In-S nanocrystals and their optical radiometric temperature sensors," *Journal of Nanoparticle Research,* vol. 21, pp. 1-8, 2019.

[35] M. Ganiga and J. Cyriac, "Understanding the photoluminescence mechanism of nitrogen-doped carbon dots by selective interaction with copper ions," *ChemPhysChem,* vol. 17, no. 15, pp. 2315-2321, 2016.

Open Access Article. Published on 24 June 2026. Downloaded on 6/29/2026 1:12:21 PM.
This article is licensed under a Creative Commons Attribution-NonCommercial 3.0 Unported Licence.

Nanoscale Accepted Manuscript

View Article Online
DOI: 10.1039/D6NR01274D

[36] V. Lyahovitskaya, Y. Feldman, K. Gartsman, H. Cohen, C. Cytermann, and D. Cahen, "Na effects on CuInSe 2: Distinguishing bulk from surface phenomena," *Journal of applied physics,* vol. 91, no. 7, pp. 4205-4212, 2002.

[37] V. Bhatt, M. Kumar, E.-C. Kim, H. J. Chung, and J.-H. Yun, "Temperature-dependent phase formation of CuInSe2 for self-biased, broadband Si/CuInSe2 heterojunction photodetector," *Journal of Alloys and Compounds,* vol. 922, p. 166190, 2022.

[38] X. Jin, T. P. Vinod, and J. Kim, "A Novel Aqueous Phase Synthetic Route for CuInSe2 Nanocrystals," *Journal of Nanoscience and Nanotechnology,* vol. 12, no. 7, pp. 5892-5896, 2012.

[39] X. Wang, F. Li, W. Li, W. Gao, Y. Tang, and R. Li, "Hollow bimetallic cobalt-based selenide polyhedrons derived from metal–organic framework: an efficient bifunctional electrocatalyst for overall water splitting," *Journal of Materials Chemistry A,* vol. 5, no. 34, pp. 17982-17989, 2017.

[40] Q.-S. Jiang *et al.*, "Electrodeposited cobalt and nickel selenides as high-performance electrocatalytic materials for dye-sensitized solar cells," *Journal of Materials Science: Materials in Electronics,* vol. 30, pp. 9429-9437, 2019.

[41] L. Pan, S. Wang, J.-J. Zou, Z.-F. Huang, L. Wang, and X. Zhang, "Ti 3+-defected and V-doped TiO 2 quantum dots loaded on MCM-41," *Chemical Communications,* vol. 50, no. 8, pp. 988-990, 2014.

[42] Z. Pu, Q. Liu, A. M. Asiri, and X. Sun, "Tungsten phosphide nanorod arrays directly grown on carbon cloth: a highly efficient and stable hydrogen evolution cathode at all pH values," *ACS applied materials & interfaces,* vol. 6, no. 24, pp. 21874-21879, 2014.

[43] X. Tong *et al.*, "Heavy metal-free, near-infrared colloidal quantum dots for efficient photoelectrochemical hydrogen generation," *Nano Energy,* vol. 31, pp. 441-449, 2017.

Open Access Article. Published on 24 June 2026. Downloaded on 6/29/2026 1:12:21 PM.
This article is licensed under a Creative Commons Attribution-NonCommercial 3.0 Unported Licence.

Nanoscale Accepted Manuscript

View Article Online
DOI: 10.1039/D6NR01274D

[44] V. González-Pedro, X. Xu, I. Mora-Sero, and J. Bisquert, "Modeling high-efficiency quantum dot sensitized solar cells," *ACS nano,* vol. 4, no. 10, pp. 5783-5790, 2010.

[45] M. D. L. Ruiz Peralta, U. Pal, and R. S. Zeferino, "Photoluminescence (PL) quenching and enhanced photocatalytic activity of Au-decorated ZnO nanorods fabricated through microwave-assisted chemical synthesis," *ACS Applied Materials & Interfaces,* vol. 4, no. 9, pp. 4807-4816, 2012.

[46] X. Chen and W. Shangguan, "Hydrogen production from water splitting on CdS-based photocatalysts using solar light," *Frontiers in Energy,* vol. 7, no. 1, pp. 111-118, 2013.

[47] F. Navarro-Pardo, H. Zhao, Z. M. Wang, and F. Rosei, "Structure/property relations in “giant” semiconductor nanocrystals: opportunities in photonics and electronics," *Accounts of chemical research,* vol. 51, no. 3, pp. 609-618, 2017.

[48] S. Zhang *et al.*, "Photocatalytic wastewater purification with simultaneous hydrogen production using MoS2 QD-decorated hierarchical assembly of ZnIn2S4 on reduced graphene oxide photocatalyst," *Water Research,* vol. 121, pp. 11-19, 2017/09/15/ 2017.

[49] K. R. Davies *et al.*, "Photoelectrocatalytic surfactant pollutant degradation and simultaneous green hydrogen generation," *Industrial & Engineering Chemistry Research,* vol. 62, no. 45, pp. 19084-19094, 2023.

[50] W. Yu, M. Xu, X. Liang, J. Wang, W. Fang, and F. Wang, "Fabrication of Ce MOFs/Black-TNTs and CCM/Black-TNTs as high-efficiency photoelectrode for wastewater treatment and hydrogen production," *Separation and Purification Technology,* vol. 303, p. 122155, 2022.

[51] C. Wang, P. Chen, H. Li, X. Cheng, J. Zhang, and M. Ni, "Photoelectrocatalytic hydrogen evolution combined with organic waste water treatment by red mud derived catalysts," *Journal of Power Sources,* vol. 661, p. 238600, 2026.

Open Access Article. Published on 24 June 2026. Downloaded on 6/29/2026 1:12:21 PM.
This article is licensed under a Creative Commons Attribution-NonCommercial 3.0 Unported Licence.

Nanoscale Accepted Manuscript

View Article Online
DOI: 10.1039/D6NR01274D

[52] J. Liu *et al.*, "Photoelectrochemical water splitting coupled with degradation of organic pollutants enhanced by surface and interface engineering of BiVO4 photoanode," *Applied Catalysis B: Environmental,* vol. 278, p. 119268, 2020.

[53] T. Annadurai *et al.*, "S-scheme N-doped carbon dots anchored g-C3N4/Fe2O3 shell/core composite for photoelectrocatalytic trimethoprim degradation and water splitting," *Applied Catalysis B: Environmental,* vol. 320, p. 121928, 2023.

[54] L. Thirumalaisamy *et al.*, "Dual shield: bifurcated coating analysis of multilayered WO3/BiVO4/TiO2/NiOOH photoanodes for sustainable solar-to-hydrogen generation from challenging waters," *ACS sustainable chemistry & engineering,* vol. 12, no. 8, pp. 3044-3060, 2024.

[55] W. Li, "Influence of electronic structures of doped TiO2 on their photocatalysis," *physica status solidi (RRL)–Rapid Research Letters,* vol. 9, no. 1, pp. 10-27, 2015.

[56] M. Swedha *et al.*, "Construction of Ag/CdZnS QDs nanocomposite for enhanced visible light photoinactivation of Staphylococcus aureus," *Environmental Pollution,* vol. 348, p. 123749, 2024.

Open Access Article. Published on 24 June 2026. Downloaded on 6/29/2026 1:12:21 PM.
This article is licensed under a Creative Commons Attribution-NonCommercial 3.0 Unported Licence.

Nanoscale Accepted Manuscript

The data supporting this article have been included as part of the Supplementary Information.

View Article Online
DOI: 10.1039/D6NR01274D

Open Access Article. Published on 24 June 2026. Downloaded on 6/29/2026 1:12:21 PM.
This article is licensed under a Creative Commons Attribution-NonCommercial 3.0 Unported Licence.

Nanoscale Accepted Manuscript